Biophysical*Journal*
Article

Biophysical Society

The SGYS motif of TAF15 prion-like domain is critical to amyloid fibril formation

Jialin Chen,[1,3,4] Xiushuang Yuan,[1] Peng Wei,[2] Daoping Wang,[3,4] Chen Chen,[1] Quanqiang Guo,[1]
Shi-Zhong Luo,[1,*] and Long Chen[1,*]
[1]Beijing Key Laboratory of Bioprocess, College of Life Science and Technology, Beijing University of Chemical Technology, Beijing, China; [2]School of Traditional Chinese Medicine, Beijing University of Chinese Medicine, Beijing, China; [3]State Key Laboratory for Functions and Applications of Medicinal Plants, Guizhou Medical University, Guiyang, China; and [4]The Key Laboratory of Chemistry for Natural Products of Guizhou Province and Chinese Academy of Sciences, Guiyang, China

ABSTRACT Misfolding of TATA-box binding protein-associated factor 15 (TAF15) may cause neurodegenerative diseases, such as amyotrophic lateral sclerosis (ALS). Some mutations of prion-like domain (PrLD) have been detected in patients with sporadic ALS, suggesting the importance of TAF15-PrLD in ALS pathogenesis. Herein, combining experiments and molecular dynamics (MD) simulations, we investigated the influences of several TAF15-PrLD mutations on the amyloid fibril formation of TAF15-PrLD-extracted peptide segments, and identified an essential β-amyloid-forming segment from TAF15-PrLD. A pathogenic mutation T2 E71G resulted in significantly enhanced aggregation of the TAF15-PrLD segment T2 (Y^{56}GQSQSGYSQSYGGYENQ^{73}). In addition, the peptide T2 with a strong β-amyloid-forming tendency was able to induce the liquid to solid phase transition of TAF15-PrLD protein. Further study identified the SGYS motif as a critical segment that promoted the formation of amyloid fibrils, which maintained a stable β-sheet structure through intermolecular hydrogen bonds and π-π stacking interaction. This work provides a clue to elucidate the molecular pathogenic mechanism of TAF15-associated neurodegenerative diseases, and will direct drug development targeting TAF15.

SIGNIFICANCE TAF15-PrLD is important in the pathogenesis of ALS. Here, combined with experiments and molecular dynamics simulations, we found that the pathogenic mutation T2 E71G can significantly increase the aggregation of TAF15-PrLD fragment T2 (Y^{56}GQSQSGYSQSYGGYENQ^{73}). In addition, peptide T2, which has a strong propensity for amyloid fibrils formation, can induce the liquid-solid phase transition of TAF15-PrLD protein. Furthermore, we also found that the SGYS motif can maintain the stability of the β-sheet structure. This motif is a key fragment that promotes the formation of amyloid fibrils. This work provides clues to elucidate the molecular pathogenesis of TAF15-related neurodegenerative diseases and will guide the development of drugs targeting TAF15.

INTRODUCTION

Neurodegenerative diseases are debilitating disorders that cause progressive degeneration and/or death of nerve cells, leading to problems in movement (called ataxia) and/or mental function (called dementia). The pathogenesis of many neurodegenerative diseases, such as Alzheimer's disease, Parkinson's disease, and amyotrophic lateral sclerosis (ALS) (1–4), are usually associated with protein misfolding and aggregation. In the process of protein aggregation, the misfolded or intrinsically disordered proteins assemble into oligomers, which then grow into amyloid-like fibrils rich in β-sheets (5–7). In most cases, the small aggregates (soluble oligomers and protofibrils) formed during amyloid aggregation are suggested as primary neurotoxic agents (8,9). Recent studies have demonstrated that many neurodegenerative disease-associated proteins can form liquid drops through liquid-liquid phase separation (LLPS), which mediates various important physiological processes (10–12). Moreover, some of them, such as FUS (13,14) and TDP-43 (15), with pathogenic mutations, have been observed to convert from liquid condensates to fibrils. In these cases, phase separation might accelerate the formation of amyloid-like fibrils (16,17).

Submitted December 7, 2021, and accepted for publication May 24, 2022.

*Correspondence: luosz@mail.buct.edu.cn or chenlong@mail.buct.edu.cn

Jialin Chen and Xiushuang Yuan contributed equally to this work.

Editor: Jianhan Chen.
https://doi.org/10.1016/j.bpj.2022.05.038

TAF15 (TATA-box binding protein-related factor 15) belongs to the FET protein family, which is a kind of RNA-binding protein (RBP). As a key regulator of RNA metabolism, TAF15 plays an important role in the physiological activities of RNA. It interacts with unphosphorylated RNA polymerase II and the components of spliceosomes, as well as auxiliary proteins, which are involved in transcription and splicing (18,19). Kapli and colleagues have also proved that TAF15 can affect mRNA stability (20). While it participates in RNA metabolism, TAF15 has been revealed to be mutated in ALS patients (21), and disease-related TAF15 mutations can lead to more severe phenotypic expression (22). These may be caused by disrupting the normal interactions between TAF15 and RNA. TAF15 is inherently easy to aggregate due to its prion-like domain (PrLD), and some studies indicated that this is the reason for pathogenicity (19,23). Evidence from in vitro studies showed that TAF15 mutants enhanced the aggregation (22). In cultured mammalian neurons, disease-related TAF15 mutations were found to induce the formation of cytoplasmic TAF15 inclusion bodies (22). However, the intrinsic molecular mechanism driving the aggregation of TAF15 has not been clearly demonstrated yet.

Approximately 70 human RBPs contain a PrLD (24), which is a low-complexity domain with a similar amino acid composition to yeast prion domains (rich in YGQSN (25)), making the protein infectious. Deletion of the PrLD eliminates protein toxicity, as well as the RNA-binding ability of TDP-43 in model organisms, suggesting its roles in both RNA engagement and protein misfolding in disease pathogenesis (26). TAF15 also contains a PrLD region at the N-terminal 1–201, which is rich in Y, G, Q, and S residues (27), and may be necessary for TAF15 aggregation (3). However, there is no resolved crystal structure of TAF15, which prevents researchers from revealing the core segments; also, the underlying mechanism for protein aggregation has not been identified yet (3).

Computer simulation, especially molecular dynamics (MD) simulation, has become an important tool to investigate the mechanism leading to protein aggregation (28–36). Currently, the computing power of supercomputers allows the simulation of complex systems with longer timescales and larger sizes to approach experimental conditions. Therefore, to demonstrate the underlying mechanism of pathogenic aggregation of TAF15, we adopted a combinational means using both MD simulation and experimental methods in this study. Because the structure and function of TAF15 are like FUS (37,38), and the sequence identity (SI) between FUS-PrLD and TAF15-PrLD is more than 50%, a homology modeling structure of TAF15-PrLD was established. Three peptide segments rich in YGQ were extracted and compared for their abilities to aggregate. The SGYS motif in TAF15-PrLD was recognized as a critical motif resulting in protein aggregation. This work provides a clue to elucidate the molecular pathogenic mechanism of TAF15-associated neurodegenerative diseases, and will be helpful for the development of targeted drugs.

MATERIALS AND METHODS

Peptide synthesis

All peptides were synthesized on a CS-Bio136 peptide synthesizer (CSBio, Menlo Park, CA, USA) using a standard Fmoc solid-phase synthesis method. Piperidine (20% v/v) was used to deprotect the Fmoc group followed by amino acid coupling using HBTU and DIPEA as coupling reagents in a molar ratio of 1:1:2 (amino acid:HBTU:DIPEA). Fmoc-protected amino acids were added in 4 equivalents of Wang resin successively according to the peptide sequence. Peptides were cleaved from resins in a mixture of TFA/TIS/water/EDT (91/3/3/3 by volume with a total of 5 mL) for 3 h. TFA solution was collected and the resin was rinsed twice with neat TFA. After TFA evaporation, the residual peptide solution was triturated with cold diethyl ether. The resulting precipitate was centrifuged and washed three times with cold diethyl ether. Crude peptides were dried under vacuum overnight and purified by reverse-phase HPLC using a binary mobile phase composed of water and acetonitrile in the presence of 0.05% TFA. Elution was monitored at 215 and 254 nm. All synthesized peptides were identified by ESI-MS (Thermo LTQ Orbitrap XL equipped with an electrospray ionization source), and their purities were assessed using analytical HPLC. Results showed that all peptides were synthesized correctly and their purities were >90% (Figs. S11 and S12).

Transmission electron microscopy

All peptides were dissolved in 10% (v/v) DMSO/DI water at a concentration of ~10 mM as stock solutions. The peptides were diluted to experimental concentrations by PBS (pH 7.4) and incubated at 37°C, 220 rpm, for 72 h and 10 μL of peptide solution was dropped onto a transmission electron microscopy (TEM) grid for 2 min to stand. The excess solution was gently wiped using filter paper. Then, 10 μL of staining reagent (2% wt sodium phosphotungstic acid aqueous solution [pH 7.0]) was added onto the grid for 2 min. The excess staining solution was wiped using filter paper. All samples were allowed to air dry overnight and imaged on an HT7700 electron microscope (Hitachi, Tokyo, Japan) at 100 kV.

Thioflavin T fluorescence assay

The peptides were diluted to 500 μM and mixed with 2 mM concentrated thioflavin T (ThT) solution to make the final concentration of ThT 20 μM. Amyloid fibril formation was detected by the enhancement of ThT fluorescence upon binding. The fibril formation detections were set up in triplicate in black 96-well round bottom plates (Corning Costar, Corning, NY, USA). Changes in ThT fluorescence were monitored at 480 nm, with 440 nm excitation, on a SpectraMax M2 plate reader (Molecular Devices, San Jose, CA, USA).

Cloning, expression, and purification of recombinant TAF15-PrLD (1–201)

His-tagged EGFP-TAF15-PrLD (1–201) was generated by standard recombinant DNA methods. The gene of EGFP-TAF15-PrLD (1–201) was cloned into pET-28a expression vector and verified by sequencing. The plasmid was transformed into Rosetta cells for protein expression followed by standard purification using nickel resins. Purified protein was desalted using elution buffer (50 mM Tris/HCl, 100 mM KCl [pH 7.4]) through a HiTrap

Desalting Column (Cytiva 17-1408-01, 5 mL) on AKTA (ÄKTA pure L 29018224-1792373).

Phase separation

For the observation of phase separation of EGFP-TAF15-PrLD (1–201) protein, 40 μM EGFP-TAF15-PrLD (1–201) solution was prepared in 10% PEG8000 with or without 1 mM pre-incubated peptide (T1/T2/T3) solution. Samples were added into a black, bottom-clear 96-well round-bottom plate (Corning Costar). Images were acquired on a Leica SP8 confocal microscope equipped with laser for 488 nm excitation using a 100× magnification objective. Samples of different incubation time were observed on a JEM-1200 electron microscope (JEOL, Tokyo, Japan) at 100 kV.

Homology modeling

The three-dimensional structure of TAF15-PrLD was predicted by a homology modeling method (through the Swiss-model (33) web site), using the PrLD of FUS (PDB: 5W3N) (28) as template (Fig. S1), whose SI to TAF15-PrLD is more than 50% (successful homology modeling requires templates with high homology, usually at least 30% SI between the target and the homologous proteins (39–41)). Protein sequence alignment between 5W3N and TAF15-PrLD was performed using the multiple sequence alignment tool ClustalW (https://www.genome.jp/tools-bin/clustalw). Three peptide segments were chosen from the PrLD region of TAF15 based on the following criteria: 1) all three peptide segments start with YGQ; 2) the three peptide segments all contain mutation sites mentioned in literature (42) (the mutation sites of T1 and T3 are detected in healthy people, and that of T2 is detected in ALS patients); 3) the length of all three peptide segments is 18 amino acids. For narrative convenience, these three segments were named T1, T2, and T3, and the peptides with mutations were correspondingly named T1 A31T, T2 E71G, and T3 Y122C (Fig. 1 *A*). The three-dimensional structures of the three peptides (T1, T2, and T3) were extracted from TAF15-PrLD, and then the peptide structure was aligned with the nine homologous peptides of the 5W3N model to obtain the initial structure of the peptide homononamers.

MD simulation with explicit solvation model

All simulation data were generated by GROMACS 2018.4 (43) software, and the system configurations were visualized using VMD software (44) and Accelrys Discovery Studio Visualizer (http://accelrys.com/products/discovery-studio/). Grace software (https://plasma-gate.weizmann.ac.il/Grace/) was used for data processing to generate pictures. Simulation system construction was carried out through the charmm-gui (45,46) web site (www.charmm-gui.org), and the force field of the peptides was CHARMM36m.

As shown in Table S1, we simulated a total of 13 systems, 11 of them are homononamers in water, 2 of them are respectively 33 T2 peptides and 33 T2 E71G peptides in water. Before determining to use 33 peptides, we have tried many times and found that at least 30 peptides are needed to make one turn of the spiral. The initial system was constructed by stacking 9 peptides head-to-tail, because the template structure (PDB: 5W3N) is an aggregate formed by 9 polypeptides. After four stacking, the three overlapping peptides were removed, and there were 33 peptides left, so we finally selected 33 peptides for the simulation. The initial box sizes of the simulation systems were determined according to the sizes of the peptides in the system (the distance between the peptides and the box boundary was 2 nm). Then, water was filled in the simulation box to dissolve the peptides. For MD simulation with periodic boundary conditions (PBCs) (47), we neutralized the charge of the system by adding positive (Na^+) or negative (Cl^-) ions as needed to avoid artifacts during the calculation of electrostatic interactions.

Energy minimizations were performed with the steepest-descent method, followed by two equilibration (EQ) steps. The position restraints for all

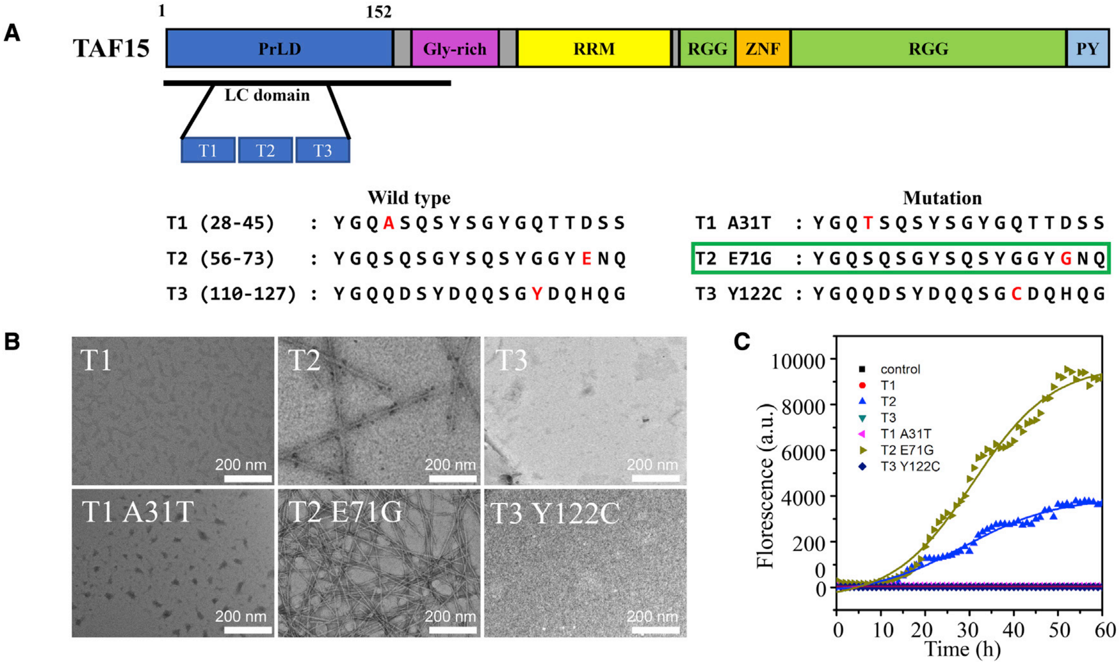

FIGURE 1 Characterization of the self-assemblies formed by T1-T3 and their mutations. (*A*) Schematic plots of the primary sequences of T1-T3 segments and their mutations extracted from TATA-binding protein-associated factor 15 (TAF15). The reported mutant residue in each segment is labeled in red. The T2 mutant T2 E71G labeled with green rectangles contains a pathogenic mutation observed in patients (42). (*B*) TEM images of T1-T3 segments and their mutants after incubation at 37°C for 72 h. (*C*) Thioflavin T (ThT) assay was performed to monitor the process of aggregation of the peptides kinetically, indicating that T2 and T2 E71G can form amyloid aggregates. To see this figure in color, go online.

nonhydrogen atoms of the peptides were imposed during the EQ steps. The first EQ step was conducted under isothermal and isochoric conditions, which was called NVT ensemble as N (the number of particles), V (the volume), and T (the temperature) are held constant. In the second EQ step, the pressure and thus the density of the system were adjusted using the iso-thermal-isobaric ensemble, also called NPT ensemble as N, P (the pressure), and T are kept constant. The NVT and NPT EQ simulations were executed for 1000 ps.

In the production run, the position restraints on the peptides were removed; however, H-bond lengths were constrained to their equilibrium values using the LINCS (48) method, which allows a time step of 2 fs for the integration of the equations of motions. The other settings of the MD production run were the same as the NPT EQ step. The nonbonded Lennard-Jones interactions were cut off at 1.2 nm. The electrostatics was treated using the particle mesh Ewald (49) scheme. All production runs were simulated in the NPT ensemble using the V-rescale (50) coupling scheme with the temperature maintained at 298.15 K and the Parrinello-Rahman (51) coupling scheme with the pressure kept at 1.0 bar and isotropic coupling type. The time constants for the pressure and temperature couplings were 2.0 and 0.2 ps, respectively, and the compressibility value was 4.5×10^{-5} bar^{-1}. The simulation time of each production simulation system was 1000 ns. The changes of RMSD (root mean-square deviation), RMSF (root mean-square fluctuation), hbnum, and secondary structure of the peptides were analyzed with time to illustrate the stability of the peptide aggregates. The RMSD values were calculated based on all the atoms, and the RMSF values were calculated based on each residue. The hydrogen bonds were counted for both main chains and side chains, and determined based on cutoffs for the angle of Hydrogen - Donor - Acceptor (zero is extended) and the distance Donor - Acceptor (or Hydrogen - Acceptor using -noda). The cutoff angle (degrees, Hydrogen - Donor - Acceptor) was 30° and the cutoff radius (nm, Donor - Acceptor) was 0.35 nm. In addition, the nonbonded interaction analysis, including both H-bonds and π-π stacking interaction, was performed on the stable homononamers, i.e., T2 and T2 E71G homononamers.

RESULTS AND DISCUSSION

The TAF15-PrLD-extracted peptide segments form amyloid fibrils

A previous study has reported that two tandem (S/G)Y(S/G) motifs of the human FUS low-complexity domain, which can form reversible fibrils, are critical for the phase separation of the protein (4). Thus, alignment analysis of their PrLD sequences were performed because TAF15 and FUS proteins have an identity of 50.81 in the PrLD region and similar functions in cells (Fig. S1 *A*). Although the three extracted peptide segments were also rich in Y, G, Q, and S residues, they had not very high identity to the corresponding segments of the FUS-PrLD (Fig. S1 *B*). T1 and T2 segments were partially overlapped with the two tandem (S/G)Y(S/G) motifs of FUS, respectively, but the sequences were not identical. All three selected peptide segments have reported mutation sites within the sequences, so that we could compare the effects of mutations on the aggregation properties. T1 A31T and T3 Y122C are nonpathogenic mutations in T1 and T3 segments, respectively, while T2 E71G is a pathogenic mutation in the T2 segment. Thus, the corresponding mutants of the three peptides, namely T1 A31T, T2 E71G, and T3 Y122C, were also synthesized for investigation.

After 72 h of incubation, the morphology of the peptide aggregates was observed by TEM. Both T2 and its mutant T2 E71G formed fibrils, while the other four peptides formed amorphous aggregates, indicating that the T2 segment has a strong aggregation ability. Notably, the fibrils formed by T2 E71G were longer than that of the wild-type T2, and the fibrils were intensively interwound (Fig. 1 *B*). On the fibrils of T2, alternative light and dark parts were observed, suggesting that the fibril had a spiral structure. Measurement on the TEM image at higher magnification showed that the pitch of the helix was ~155 nm. Details of the images indicated that the fibril was a bundle belt with several single sheets arranged side by side, and the observed number of strands ranged from 2 to 6 (Fig. S2). Similarly, T2 E71G fibrils also displayed a helical structure, and the pitch of the helix was estimated to be ~95 nm (Fig. S2). The pitch of the T2 E71G fibril was shorter than that of T2 fibril, suggesting that the assembly of T2 E71G was more compact than T2.

To further demonstrate the possible structures of the fibrils, we constructed an initial structure of assembly with 33 peptide molecules for MD simulation, which was arranged in parallel according to the arrangement of the homononamer peptide of the homologous FUS model (PDB: 5W3N). After 100 ns simulation, the T2 assembly structure eventually evolved to a left-handed spiral structure (Fig. S3) with a diameter of 2.795 nm, while the TEM observed bundle fibril was right handed (Fig. S2), which might be because the simulated aggregate structure of the peptides was only one of the sheets of the TEM observed fiber (Fig. S2 *A*). If we carefully observed the detailed assembly structures of T2 fibril, we could find that the fibril was composed of multiple sheets, and the diameter of each sheet (~2.4 nm) was close to the simulated fibrils. Therefore, we conjectured that T2 or T2 E71G peptides formed single sheets first, and then further assembled into bundle fibrils that observed by TEM. This could possibly explain the different sizes of experiments and simulation.

The aggregating ability of these peptides were also monitored for their β-amyloid-forming processes using the ThT assay. Time-dependent increases in the ThT fluorescence were observed only in T2 and T2 E71G peptide solution, suggesting that only these two peptide segments formed β-amyloid aggregates (Fig. 1 *C*). In particular, the fluorescence intensity of T2 E71G was much higher and increased much faster than that of T2, which meant that T2 E71G aggregated more rapidly. Both TEM and ThT results indicate that T2 and its mutant T2 E71G can form amyloid fibrils, while the other peptides have no obvious aggregation. Thus, T2 could be an important segment driving the aggregation of TAF15-PrLD.

The peptide segment T2 promotes liquid- to solid-phase transition of TAF15-PrLD

PrLD has been reported to enable RBPs to undergo LLPS, which underlies the formation of membraneless organelles, and irreversible liquid to solid transition of RBPs may result in cytotoxicity on neurons (42). The PrLD of TAF15 is believed to be responsible for the dynamic assembly of this protein, thus the seeding effect of the three extracted peptide segments on TAF15-PrLD were detected to further demonstrate their abilities to induce protein aggregation. Pre-incubated peptides T1, T2, and T3 were incubated with TAF15-PrLD for 6 h to determine whether they can induce TAF15-PrLD aggregation. LLPS of TAF15-PrLD was observed by both confocal microscope and TEM, as it can form globular liquid droplets in 10% PEG. When incubated with T2 fibril seed, amorphous aggregation of TAF15-PrLD protein was observed after 6 h incubation. By contrast, the LLPS state of TAF15-PrLD had no obvious change when it was incubated with T1 and T3 seeds (Fig. 2). This indicated that the T2 segment promoted the LLPS state to aggregation state transition of TAF15-PrLD, and that the T2 segment is essential for the aggregation of TAF15 protein.

The phenomenon that PrLD peptide segments induce the transition of LLPS protein droplets to fibrils has also been reported in FUS (4,14) and TDP-43 (52,53). It is believed that LLPS is a dynamically reversible state in cells to exert biological functions but, once the protein aggregate forms, the process becomes irreversible and may cause cytotoxicity (54,55). Therefore, when mutation occurs in the β-amyloid-forming segment of TAF15-PrLD, such as the pathogenic mutation T2 E71G, which promotes protein aggregation, it may result in cytotoxicity to neurons and cause degenerative diseases.

The T2 peptide segment can form stable assembly by MD simulation

MD simulation has been applied to study the process of peptide self-assembling and inspires the understanding of the underlying mechanisms (56,57). To get insight into the molecular mechanism of self-assembling of the TAF15-PrLD peptide segments, homononamer peptides were constructed by homology modeling and MD simulation was performed. After three 1000 ns scale simulations, the RMSD of the peptide assembly was analyzed. As shown in Fig. 3, T2 and T2 E71G homononamers maintained relatively stable RMSD values, and that of T2 E71G homononamer had the least fluctuation among these peptides. The RMSD values of T1, T1 A31T, T3, and T3 Y122C homononamers all increased during the MD simulation. Correspondingly, the structures of the homononamers of T2 and T2 E71G maintained a relatively regular conformation, while the structures of T1, T1 A31T, T3, and T3 Y122C homononamers changed a lot or even dissembled. As for RMSF, T2 and T2 E71G had small values, and the difference between each peptide in the homononamer was relatively small. By contrast, the RMSF values of the other peptides and the difference between the peptide molecules in each homononamer were much greater (Fig. S4). All these results indicate that T2 and T2 E71G can form stable self-assemblies, but the other peptides cannot. The simulation results are consistent with the experiments, and thus the simulation system should be suitable for the analysis of aggregation mechanism of the peptides.

Intermolecular hydrogen bonds maintain the β-sheet structure of the peptide assemblies

From the simulation results, an obvious change in the secondary structure of each peptide molecules in the homononamer was observed (Fig. 3), thus detailed analysis in the secondary structure of each residue in the homononamer peptides was performed. The β-sheet and β-bridge structures in T2 and T2 E71G homononamers maintained well throughout the simulation, and the β-sheet content of T2 E71G was more than that of T2. However, the other

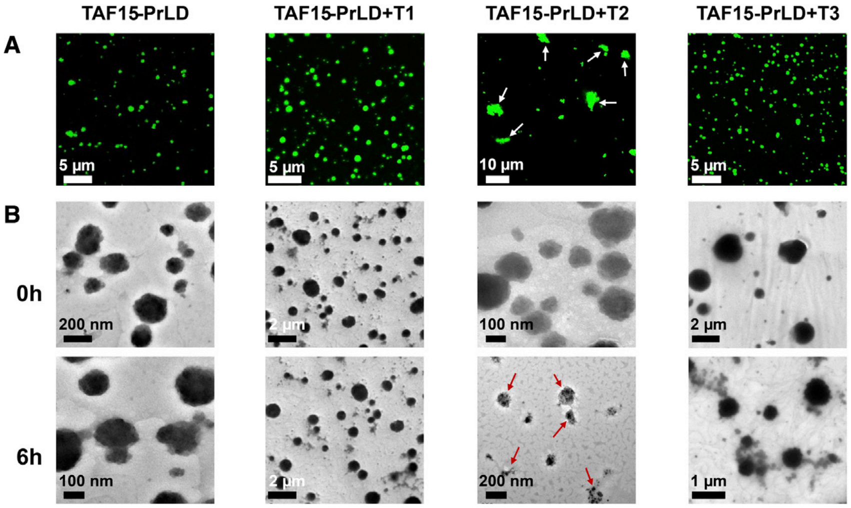

FIGURE 2 The peptide T2 promoted TAF15-PrLD transition from liquid to solid state. (*A*) Observation of the LLPS or aggregation of enhanced green fluorescent protein fused TAF15-PrLD (EGFP-TAF15-PrLD) by confocal microscopy. EGFP-TAF15-PrLD were mixed with pre-incubated peptides T1, T2, and T3, and incubated for 6 h in 10% polyethylene glycol (PEG). Aggregates are indicated by white arrows. (*B*) TEM images of EGFP-TAF15-PrLD LLPS droplets or aggregates before and after incubation with pre-incubated peptides T1, T2, and T3 in 10% PEG. Aggregates are indicated by red arrows. To see this figure in color, go online.

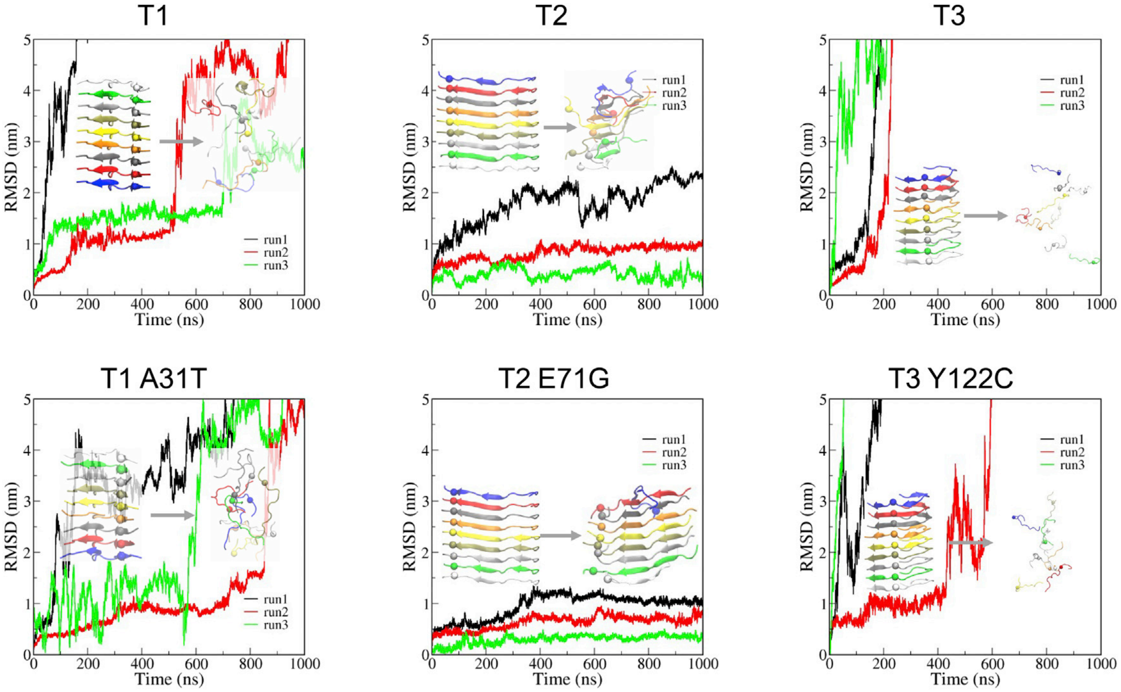

FIGURE 3 The RMSD of the peptide homononamers and the corresponding structural changes after 1000 ns MD simulation. Insets are the structures of the peptide homononamers at 0 and 1000 ns of MD simulation, which are displayed in NewCartoon mode and labeled with different colors for various peptides. The Cα values of the residues relevant to the mutation are indicated by spheres. To see this figure in color, go online.

homononamers tended to become random coil structures eventually (Fig. 4). As shown in Fig. S5, S^{61}GYS^{64} in both T2 and T2 E71G homononamers had the highest ratio of β-sheet, while there is no residue with the ratio of the β-sheet exceeding 0.5 in the T1, T1 A31T, T3, and T3 Y122C systems. It seemed that the stable T2 and T2 E71G peptide assemblies were favored by the high content of β-sheets, which is beneficial for the formation of intermolecular hydrogen bonds.

As the three extracted peptide segments are rich in polar residues, the number of hydrogen bonds in each homononamer was analyzed (Fig. S6). This showed that the number of hydrogen bonds in T2 and T2 E71G homononamers could be maintained at a certain number, while that in the other peptide homononamer systems continuously decreased (Fig. S6). Among all the peptide homononamers, T2 E71G homononamers had the most hydrogen bond number and the least fluctuation. In addition, the π-π interaction

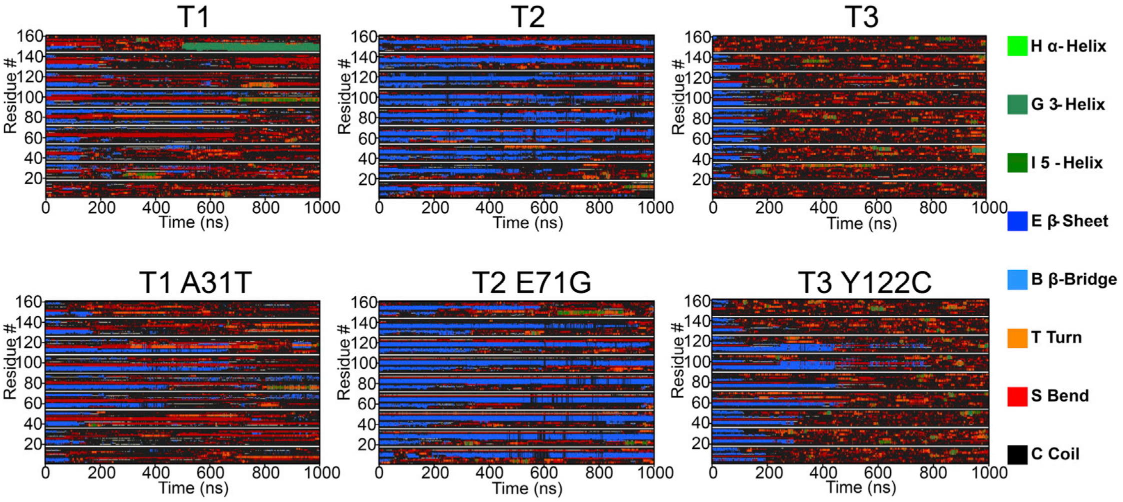

FIGURE 4 Changes in the secondary structures of different homononamer peptides. The ordinate is greater than 160 because each polypeptide has 18 amino acid residues; thus 9 peptides have a total of 162 amino acid residues. To see this figure in color, go online.

between peptide molecules were also analyzed, and only that of Y70-Y70 was increased obviously in T2 E71G. However, the number of π-π interaction between the peptides was much less than that of hydrogen bonds (Fig. S7). This suggests that the hydrogen bonds between peptide molecules might be the main forces to maintain T2 and T2 E71G assemblies, which is in accordance with the formation of β-sheet structure.

The SGYS motif with β-strand structure is critical for the amyloid aggregate formation

To further determine the critical segments involved in the peptide aggregation, the secondary structures of the peptides were further analyzed. As T2, containing only the β-strand SGYS motif, could form amyloid fibrils (Fig. 5 *A*), the SGYS motif was believed to be critical for the peptide and protein aggregation. Comparing the sequences of the three extracted peptides T1, T2, and T3, it was found that T1 and T3 contained similar fragments to the SGYS motif, which were SGYG in T1 and SGYD in T3 (Fig. 1 *A*). To illustrate the importance of the SGYS motif, two mutations, T1 G39S and T3 D123S, were constructed to introduce the SGYS motif to the peptides. As shown in Fig. 6, the RMSD values of T1 G39S and T3 D123S homononamers were very stable, in comparison to those of T1 and T3 homononamers, which changed greatly. To more directly demonstrate the importance of the SGYS fragment in the T2 peptide, we constructed three T2-related mutations, T2 S64D, T2 S64G, and T2 ΔSGYS, to eliminate the SGYS in the

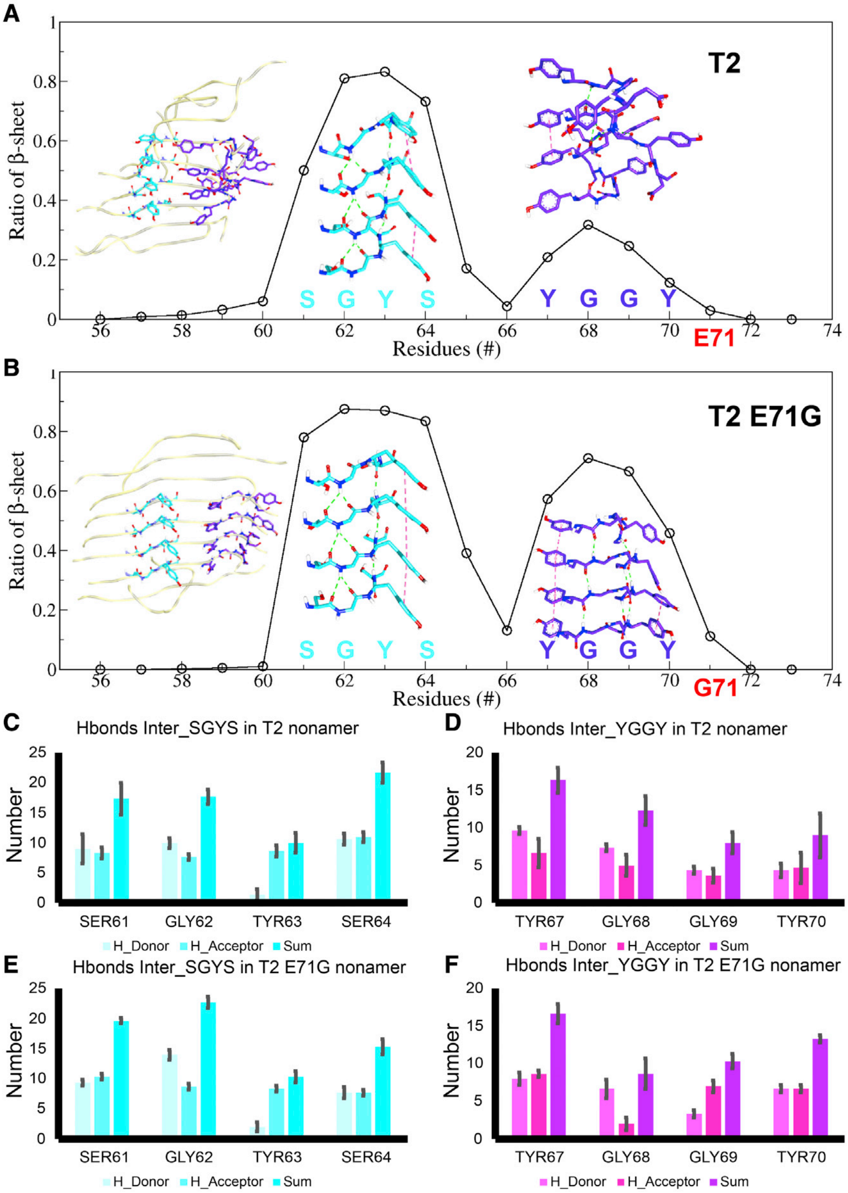

FIGURE 5 The importance of $S^{61}GYS^{64}$ in maintaining the stable aggregation structure of the peptides. (*A*) $S^{61}GYS^{64}$ of T2 is the motif with the highest ratio of β-sheets. The structure of the SGYS amino acid fragments (C atoms are colored *cyan*) in the four peptides in the middle of the T2 nonamer is relatively regular, but YGGY (C atoms are colored *modena*) is not. The hydrogen bonds and π-π stacking interaction are mainly formed between SGYS fragments. However, in YGGY fragments, only a few hydrogen bonds and π-π stacking interactions are formed. The snapshots are the structural representation of the SGYS and YGGY amino acid fragment in the four peptides in the middle of the T2 nonamer after 1000 ns. (*B*) $S^{61}GYS^{64}$ of T2 E71G is the motif with the highest ratio of β-sheets, and the YGGY segment, which nears the mutation site, shows an increase of the β-sheet ratio compared with the YGGY segment in T2. The structure of the SGYS fragments in the four peptides in the middle of the T2 E71G nonamer is relatively regular, as is YGGY. The hydrogen bonds and π-π stacking interaction are mainly formed between SGYS and YGGY fragments. The green dashed line is hydrogen bonding, and the purple dashed line is π-π stacking interaction. The snapshots are the structural representation of the SGYS and YGGY fragments in the four peptides in the middle of the T2 E71G nonamer after 1000 ns. (*C* and *E*) The number of hydrogen bonds formed between each residue of the $S^{61}GYS^{64}$ motif and all other residues in (*C*) the T2 and (*E*) the T2 E71G homononamers. (*D* and *F*) The number of hydrogen bonds formed between each residue of the $Y^{67}GGY^{70}$ fragment and all other amino acids in (*D*) the T2 and (*F*) the T2 E71G homononamers. The hydrogen bonding data in the (*D*), (*E*), (*F*), and (*G*) histograms are from nonamer structures every 100 ns from 100 to 1000 ns (10 structures in total) during the simulation. The error bar data come from the standard deviation of the data of the 10 structures. To see this figure in color, go online.

peptide. As shown in Fig. S8 *A*, the nonamers of these mutant peptides could not maintain stable aggregate structures within the simulation period of 1000 ns. In the ThT experiment, the fluorescence intensities of these mutant peptide solution did not increase within 70 h of incubation (Fig. S8 *B*), indicating that none of them can form amyloid aggregates. The observation by TEM showed that these mutant peptides could not form fibril structures after incubation (Fig. S8 *C*). As shown in Fig. S9, the β-sheet content of each residue in the three mutant peptides, T2 S64D, T2 S64G, and T2 ΔSGYS, was very low. More obviously, there was almost no residue in the T2 ΔSGYS peptide form β-sheet structure. These results indicate that the SGYS motif mainly adopts β-sheet structure in the peptides and it is critical for maintaining a stable assembly structure.

The SGYS motif has been identified only in a few proteins, such as scorpion toxins TsVII, TsNTxP, and TsIV (58), and FUS proteins. In a previous study on the FUS protein, two tandem (S/G)Y(S/G) motifs, S^{37}YSGYS^{42} (RAC1) and S^{54}YSSYG^{59} (RAC2), have been identified as reversible amyloid cores that mediate the dynamic assembly of FUS-PrLD. The RAC1 motif also contains the SGYS segment, but its assembly structure features an ordered-coil fibril spine rather than the extended β-strand typical of amyloids, which is maintained by the hydrogen bond network of both backbones and side chains, as well as the π-π stacking of Tyr38(4). Thus, the nonbonded interaction of the SGYS motif in the T2 homononamer was analyzed to compare the contribution of each residue in this motif (Fig. 5 *A*). By analyzing the number of hydrogen bonds that each residue involved, Ser64 was found to form the most hydrogen bonds with other residues (including Ser64 of another peptide molecule) in the T2 homononamer (Fig. 5 *C*). In addition, π-π stacking (Fig. S10, π-π interactions are determined by the following tests: $R_{cen} \leq 6$ Å and $R_{clo} \leq 4.5$ Å and $\theta \leq 50°$ and $\gamma \leq 35$) of Tyr63 was also involved in stabilizing the assembly structure (Fig. 5 *A* and S7 *A*).

Considering that T2 E71G contains a pathogenic mutation (1), the results from experiments and MD simulation both suggest that the pathogenesis might result from the enhanced tendency to induce TAF15 aggregation. Analysis of the structure changes of T2 E71G showed that the ratio of β-sheets (Fig. 5 *B*) and the number of hydrogen bonds (Fig. 5 *F*) in the YGGY segment increased a lot, compared with that in the peptide T2. Meanwhile, the ratio of β-sheets and the number of hydrogen bonds in the SGYS motif also increased slightly, but the contribution of each residue changed a lot, as the number of hydrogen bonds involved by S61 and G62 greatly increased in the T2 E71G peptide (Fig. 5 *E*). Hence, T2 E71G peptide had a longer β-strand segment than the wild-type T2 peptide, and formed more hydrogen bonds in the homononamer (Fig. S5). The structure change of the peptide is due to the mutation of E to G, which favored the β-strand formation of the nearby segment YGGY. The π-π stacking interaction of the YGGY segment also increased significantly in T2 E71G, compared with peptide T2, which may also contribute to the formation of amyloid aggregates (Fig. S7 *B*). Therefore,

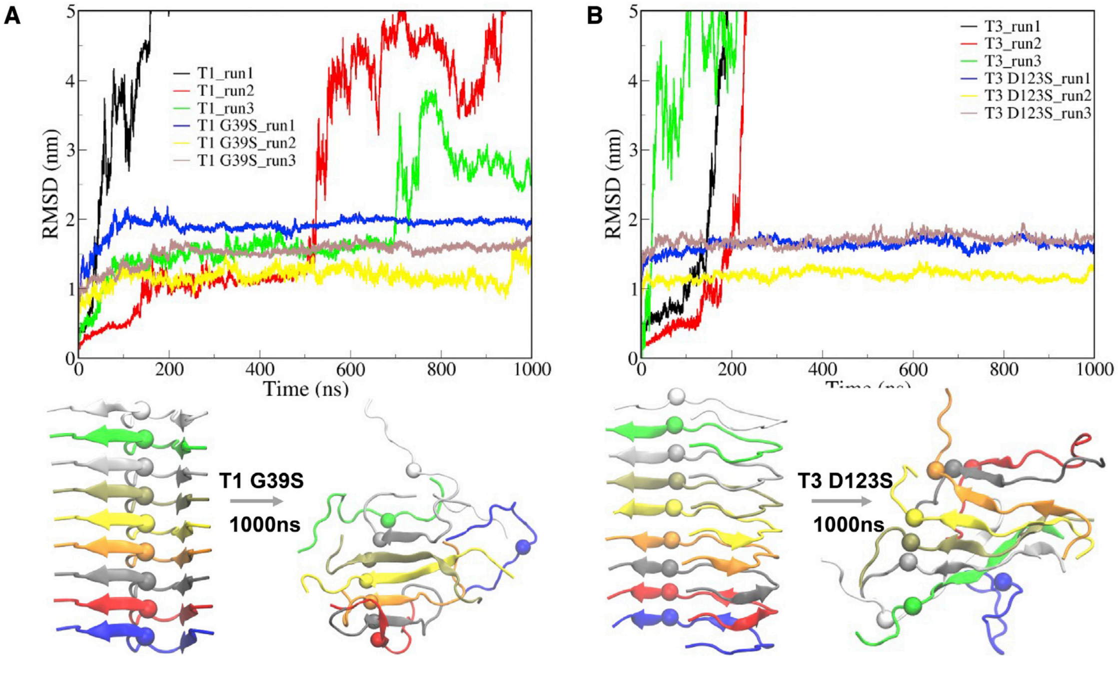

FIGURE 6 The RMSD of the homononamers of (*A*) T1 and T1 G39S and (*B*) T3 and T3 D123S. Subjacent are the corresponding initial structure and the structure at 1000 ns of the mutant peptides. The Cα values of the residues relevant to the mutation are indicated by spheres. To see this figure in color, go online.

the SGYS motif in TAF15-PrLD may be critical for mediating the dynamic assembly of TAF15 for normal functions, but the pathogenic mutation of E71G promoted the formation of amyloid aggregates of the protein, and thus result in neurodegenerative diseases.

MD simulation is a well-established technique for classical simulations of all-atom systems on nanosecond timescales; however, for complex systems, long-term simulations are still in their infancy. In this study, we first gave the regular sheet structure of the peptide through homology modeling, and then used this structure as the initial structure for subsequent MD simulations. As a result, the simulation process lacks the assembling process of peptides from disordered structures to ordered structures (this process often takes a very long time, and conventional all-atom MD simulations are difficult to achieve). Although the simulation is not the real assembling process, we can also illustrate the aggregation stability of the peptides by analyzing whether the peptides can maintain the ordered structure. Therefore, combining with the experimental results, we can conclude that the SGYS motif with β-sheet structure is critical for the amyloid fibril formation.

CONCLUSIONS

This study determined the SGYS motif as a critical amyloid fibril-forming segment in the TAF15-PrLD, mediating protein assembly. The SGYS motif containing segment T2 (YGQSQSGYSQSYGGYENQ) formed amyloid fibril maintained by the intermolecular hydrogen bonds of the β-sheet structure. The pathogenic mutation T2 E71G was demonstrated to promote peptide fibril formation by maintaining more stable β-sheet structures via more hydrogen bonds and π-π stacking. Therefore, mutation in the essential β-amyloid-forming segments of TAF15-PrLD, which promotes the aggregation of the protein, might be one of the reasons for the pathogenesis of TAF15-associated neurodegenerative diseases. This study contributes to understanding the molecular mechanism of TAF15 protein aggregation, and provides a clue for the targeted drug development of TAF15-associated neurodegenerative diseases.

SUPPORTING MATERIAL

Supporting material can be found online at https://doi.org/10.1016/j.bpj.2022.05.038.

AUTHOR CONTRIBUTIONS

J.C. designed this study, performed the molecular dynamic simulations, analyzed the simulation data, and wrote the article. X.Y. performed the experiments and analyzed the experimental data. P.W. provided part of computing resources. D.W. provided some computing resources and suggested the arrangement of Fig. 6. C.C. and Q.G. performed part of the experiments. L.C. and S.-Z.L. designed this study, analyzed the data, and revised the article.

ACKNOWLEDGMENTS

This work was supported by the National Natural Science Foundation of China (22077010); the National Key Research and Development Program of China (2021YFC2103900); the Military Biosecurity Research Program (19SWAQ06); the Joint Project of BRC-BC (Biomedical Translational Engineering Research Center of BUCT-CJFH) (XK2022-07, XK2020-09).

DECLARATION OF INTERESTS

The authors declare no competing interests.

REFERENCES

1. Ticozzi, N., C. Vance, …, J. Landers. 2011. Mutational analysis reveals the FUS homolog TAF15 as a candidate gene for familial amyotrophic lateral sclerosis. *Am. J. Med. Genet. B Neuropsychiatr. Genet.* 156:285–290. https://doi.org/10.1002/ajmg.b.31158.
2. Li, Y. Q., M. S. Tan, …, L. Tan. 2016. Frontotemporal lobar degeneration: mechanisms and therapeutic strategies. *Mol. Neurobiol.* 53:6091–6105. https://doi.org/10.1007/s12035-015-9507-5.
3. Svetoni, F., P. Frisone, and M. P. Paronetto. 2016. Role of FET proteins in neurodegenerative disorders. *RNA Biol.* 13:1089–1102. https://doi.org/10.1080/15476286.2016.1211225.
4. Luo, F., X. Gui, …, C. Liu. 2018. Atomic structures of FUS LC domain segments reveal bases for reversible amyloid fibril formation. *Nat. Struct. Mol. Biol.* 25:341–346. https://doi.org/10.1038/s41594-018-0050-8.
5. Yang, W., J. R. Dunlap, …, R. Wetzel. 2002. Aggregated polyglutamine peptides delivered to nuclei are toxic to mammalian cells. *Hum. Mol. Genet.* 11:2905–2917. https://doi.org/10.1093/hmg/11.23.2905.
6. Chen, S. M., F. A. Ferrone, and R. Wetzel. 2002. Huntington's disease age-of-onset linked to polyglutamine aggregation nucleation. *Proc. Natl. Acad. Sci. U S A.* 99:11884–11889. https://doi.org/10.1073/pnas.182276099.
7. Scherzinger, E., A. Sittler, …, E. E. Wanker. 1999. Self-assembly of polyglutamine-containing huntingtin fragments into amyloid-like fibrils: implications for Huntington's disease pathology. *Proc. Natl. Acad. Sci. U S A.* 96:4604–4609. https://doi.org/10.1073/pnas.96.8.4604.
8. Kayed, R., E. Head, …, C. G. Glabe. 2003. Common structure of soluble amyloid oligomers implies common mechanism of pathogenesis. *Science.* 300:486–489. https://doi.org/10.1126/science.1079469.
9. Straub, J. E., and D. Thirumalai. 2011. Toward a molecular theory of early and late events in monomer to amyloid fibril formation. *Annu. Rev. Phys. Chem.* 62:437–463. https://doi.org/10.1146/annurev-physchem-032210-103526.
10. Ray, S., N. Singh, …, S. K. Maji. 2020. α-Synuclein aggregation nucleates through liquid–liquid phase separation. *Nat. Chem.* 12:705–716. https://doi.org/10.1038/s41557-020-0465-9.
11. Alberti, S., A. Gladfelter, and T. Mittag. 2019. Considerations and challenges in studying liquid-liquid phase separation and biomolecular condensates. *Cell.* 176:419–434. https://doi.org/10.1016/j.cell.2018.12.035.
12. Boyko, S., K. Surewicz, and W. K. Surewicz. 2020. Regulatory mechanisms of tau protein fibrillation under the conditions of liquid-liquid phase separation. *Proc. Natl. Acad. Sci. U S A.* 117:31882–31890. https://doi.org/10.1073/pnas.2012460117.
13. Patel, A., H. O. Lee, …, S. Alberti. 2015. A liquid-to-solid phase transition of the ALS protein FUS accelerated by disease mutation. *Cell.* 162:1066–1077. https://doi.org/10.1016/j.cell.2015.07.047.
14. Ding, X., F. Sun, …, S. Z. Luo. 2020. Amyloid-forming segment induces aggregation of FUS-LC domain from phase separation

modulated by site-specific phosphorylation. *J. Mol. Biol.* 432:467–483. https://doi.org/10.1016/j.jmb.2019.11.017.

15. Conicella, A. E., G. H. Zerze, …, N. L. Fawzi. 2016. ALS mutations disrupt phase separation mediated by alpha-helical structure in the TDP-43 low-complexity C-terminal domain. *Structure.* 24:1537–1549. https://doi.org/10.1016/j.str.2016.07.007.
16. Molliex, A., J. Temirov, …, J. Taylor. 2015. Phase separation by low complexity domains promotes stress granule assembly and drives pathological fibrillization. *Cell.* 163:123–133. https://doi.org/10.1016/j.cell.2015.09.015.
17. Pak, C. W., M. Kosno, …, M. Rosen. 2016. Sequence determinants of intracellular phase separation by complex coacervation of a disordered protein. *Mol. Cell.* 63:72–85. https://doi.org/10.1016/j.molcel.2016.05.042.
18. Kapeli, K., F. J. Martinez, and G. W. Yeo. 2017. Genetic mutations in RNA-binding proteins and their roles in ALS. *Hum. Genet.* 136:1193–1214. https://doi.org/10.1007/s00439-017-1830-7.
19. Kwon, I., M. Kato, …, S. McKnight. 2013. Phosphorylation-regulated binding of RNA polymerase II to fibrous polymers of low-complexity domains. *Cell.* 155:1049–1060. https://doi.org/10.1016/j.cell.2013.10.033.
20. Kapeli, K., G. A. Pratt, …, G. W. Yeo. 2016. Distinct and shared functions of ALS-associated proteins TDP-43, FUS and TAF15 revealed by multisystem analyses. *Nat. Commun.* 7:12143. https://doi.org/10.1038/ncomms12143.
21. Neumann, M., E. Bentmann, …, I. R. A. Mackenzie. 2011. FET proteins TAF15 and EWS are selective markers that distinguish FTLD with FUS pathology from amyotrophic lateral sclerosis with FUS mutations. *Brain.* 134:2595–2609. https://doi.org/10.1093/brain/awr201.
22. Couthouis, J., M. P. Hart, …, A. D. Gitler. 2012. Evaluating the role of the FUS/TLS-related gene EWSR1 in amyotrophic lateral sclerosis. *Hum. Mol. Genet.* 21:2899–2911. https://doi.org/10.1093/hmg/dds116.
23. Yang, L., J. Gal, …, H. Zhu. 2014. Self-assembled FUS binds active chromatin and regulates gene transcription. *Proc. Natl. Acad. Sci. U S A.* 111:17809–17814. https://doi.org/10.1073/pnas.1414004111.
24. March, Z. M., O. D. King, and J. Shorter. 2016. Prion-like domains as epigenetic regulators, scaffolds for subcellular organization, and drivers of neurodegenerative disease. *Brain Res.* 1647:9–18. https://doi.org/10.1016/j.brainres.2016.02.037.
25. Toombs, J. A., B. R. McCarty, and E. D. Ross. 2010. Compositional determinants of prion formation in yeast. *Mol. Cell Biol.* 30:319–332. https://doi.org/10.1128/mcb.01140-09.
26. Ash, P. E., Y. J. Zhang, …, C. D. Link. 2010. Neurotoxic effects of TDP-43 overexpression in C. elegans. *Hum. Mol. Genet.* 19:3206–3218. https://doi.org/10.1093/hmg/ddq230.
27. Sun, Z., Z. Diaz, …, A. D. Gitler. 2011. Molecular determinants and genetic modifiers of aggregation and toxicity for the ALS disease protein FUS/TLS. *PLoS Biol.* 9:e1000614. https://doi.org/10.1371/journal.pbio.1000614.
28. Carballo-Pacheco, M., and B. Strodel. 2016. Advances in the simulation of protein aggregation at the atomistic scale. *J. Phys. Chem. B.* 120:2991–2999. https://doi.org/10.1021/acs.jpcb.6b00059.
29. Dror, R. O., R. M. Dirks, …, D. E. Shaw. 2012. Biomolecular simulation: a computational microscope for molecular biology. *Annu. Rev. Biophys.* 41:429–452. https://doi.org/10.1146/annurev-biophys-042910-155245.
30. Owen, M. C., D. Gnutt, …, B. Strodel. 2019. Effects of *in vivo* conditions on amyloid aggregation. *Chem. Soc. Rev.* 48:3946–3996. https://doi.org/10.1039/c8cs00034d.
31. Redler, R. L., D. Shirvanyants, …, N. V. Dokholyan. 2014. Computational approaches to understanding protein aggregation in neurodegeneration. *J. Mol. Cell Biol.* 6:104–115. https://doi.org/10.1093/jmcb/mju007.
32. Wei, G., N. Mousseau, and P. Derreumaux. 2007. Computational simulations of the early steps of protein aggregation. *Prion.* 1:3–8. https://doi.org/10.4161/pri.1.1.3969.
33. Wen, J., D. R. Scoles, and J. C. Facelli. 2017. Molecular dynamics analysis of the aggregation propensity of polyglutamine segments. *PLoS One.* 12:e0178333. https://doi.org/10.1371/journal.pone.0178333.
34. Galm, L., S. Amrhein, and J. Hubbuch. 2017. Predictive approach for protein aggregation: correlation of protein surface characteristics and conformational flexibility to protein aggregation propensity. *Biotechnol. Bioeng.* 114:1170–1183. https://doi.org/10.1002/bit.25949.
35. Grassmann, G., M. Miotto, …, E. Milanetti. 2021. A computational approach to investigate TDP-43 RNA-recognition motif 2 C-terminal fragments aggregation in amyotrophic lateral sclerosis. *Biomolecules.* 11:1905. https://doi.org/10.3390/biom11121905.
36. Ng, Y. K., N. N. Tajoddin, …, L. Konermann. 2021. Mechanism of thermal protein aggregation: experiments and molecular dynamics simulations on the high-temperature behavior of myoglobin. *J. Phys. Chem. B.* 125:13099–13110. https://doi.org/10.1021/acs.jpcb.1c07210.
37. King, O. D., A. D. Gitler, and J. Shorter. 2012. The tip of the iceberg: RNA-binding proteins with prion-like domains in neurodegenerative disease. *Brain Res.* 1462:61–80. https://doi.org/10.1016/j.brainres.2012.01.016.
38. Couthouis, J., M. P. Hart, …, A. D. Gitler. 2011. A yeast functional screen predicts new candidate ALS disease genes. *Proc. Natl. Acad. Sci. U S A.* 108:20881–20890. https://doi.org/10.1073/pnas.1109434108.
39. Modi, V., Q. Xu, …, R. L. Dunbrack, Jr. 2016. Assessment of template-based modeling of protein structure in CASP11. *Proteins.* 84:200–220. https://doi.org/10.1002/prot.25049.
40. Kryshtafovych, A., B. Monastyrskyy, …, A. Tramontano. 2018. Evaluation of the template-based modeling in CASP12. *Proteins.* 86:321–334. https://doi.org/10.1002/prot.25425.
41. Baker, D., and A. Sali. 2001. Protein structure prediction and structural genomics. *Science.* 294:93–96. https://doi.org/10.1126/science.1065659.
42. Harrison, A. F., and J. Shorter. 2017. RNA-binding proteins with prion-like domains in health and disease. *Biochem. J.* 474:1417–1438. https://doi.org/10.1042/bcj20160499.
43. Abraham, M. J., T. Murtola, …, E. Lindahl. 2015. GROMACS: high performance molecular simulations through multi-level parallelism from laptops to supercomputers. *SoftwareX.* 1-2:19–25. https://doi.org/10.1016/j.softx.2015.06.001.
44. Humphrey, W., A. Dalke, and K. Schulten. 1996. VMD: visual molecular dynamics. *J. Mol. Graph.* 14:33–38. https://doi.org/10.1016/0263-7855(96)00018-5.
45. Lee, J., X. Cheng, …, W. Im. 2015. CHARMM-GUI input generator for NAMD, GROMACS, AMBER, OpenMM, and CHARMM/OpenMM simulations using the CHARMM36 additive force field. *J. Chem. Theor. Comput.* 12:405–413. https://doi.org/10.1021/acs.jctc.5b00935.
46. Jo, S., T. Kim, …, W. Im. 2008. CHARMM-GUI: a web-based graphical user interface for CHARMM. *J. Comput. Chem.* 29:1859–1865. https://doi.org/10.1002/jcc.20945.
47. Bekker, H., J. P. van den Berg, and T. A. Wassenaar. 2004. A method to obtain a near-minimal-volume molecular simulation of a macromolecule, using periodic boundary conditions and rotational constraints. *J. Comput. Chem.* 25:1037–1046. https://doi.org/10.1002/jcc.20050.
48. Hess, B. 2008. P-LINCS: A parallel linear constraint solver for molecular simulation. *J. Chem. Theor. Comput.* 4:116–122. https://doi.org/10.1021/ct700200b.
49. Kawata, M., and U. Nagashima. 2001. Particle mesh Ewald method for three-dimensional systems with two-dimensional periodicity. *Chem. Phys. Lett.* 340:165–172. https://doi.org/10.1016/s0009-2614(01)00393-1.
50. Bussi, G., D. Donadio, and M. Parrinello. 2007. Canonical sampling through velocity rescaling. *J. Chem. Phys.* 126, 014101. https://doi.org/10.1063/1.2408420.
51. Carretero-González, R., P. G. Kevrekidis, …, D. J. Frantzeskakis. 2005. A Parrinello-Rahman approach to vortex lattices. *Phys. Lett.* 341:128–134. https://doi.org/10.1016/j.physleta.2005.04.046.

52. Saini, A., and V. S. Chauhan. 2011. Delineation of the core aggregation sequences of TDP-43 C-terminal fragment. *Chembiochem.* 12:2495–2501. https://doi.org/10.1002/cbic.201100427.

53. Babinchak, W. M., R. Haider, …, W. K. Surewicz. 2019. The role of liquid-liquid phase separation in aggregation of the TDP-43 low-complexity domain. *J. Biol. Chem.* 294:6306–6317. https://doi.org/10.1074/jbc.ra118.007222.

54. Wang, K., J. Q. Liu, …, Y. Liang. 2020. Phase separation and cytotoxicity of tau are modulated by protein disulfide isomerase and S-nitrosylation of this molecular chaperone. *J. Mol. Biol.* 432:2141–2163. https://doi.org/10.1016/j.jmb.2020.02.013.

55. Monahan, Z., V. H. Ryan, …, N. L. Fawzi. 2017. Phosphorylation of the FUS low-complexity domain disrupts phase separation, aggregation, and toxicity. *EMBO J.* 36:2951–2967. https://doi.org/10.15252/embj.201696394.

56. Zhang, Z., H. Chen, …, L. Lai. 2007. Molecular dynamics simulations on the oligomer-formation process of the GNNQQNY peptide from yeast prion protein Sup35. *Biophys. J.* 93:1484–1492. https://doi.org/10.1529/biophysj.106.100537.

57. Yang, J., M. V. Agnihotri, …, S. J. Singer. 2021. A theoretical study of polymorphism in VQIVYK fibrils. *Biophys. J.* 120:1396–1416. https://doi.org/10.1016/j.bpj.2021.01.032.

58. Alvarenga, L. M., R. A. Machado de Avila, …, C. Chávez-Olórtegui. 2005. Molecular characterization of a neutralizing murine monoclonal antibody against Tityus serrulatus scorpion venom. *Toxicon.* 46:664–671. https://doi.org/10.1016/j.toxicon.2005.07.014.